Revealing slip-induced extension twinning behaviors dominated by micro deformation in a magnesium alloy

Bijin Zhou[a,b], Leyun Wang[a], Peipeng Jin[c], Hailong Jia[b,d], Hans Jørgen Roven[b], Xiaoqin Zeng [a,e*], Yanjun Li[b*]

[a]National Engineering Research Center of Light Alloy Net Forming, Shanghai Jiao Tong University, Shanghai 200240, China

[b]Department of Materials Science and Engineering, Norwegian University of Science and Technology, Trondheim 7491, Norway

[c]School of Mechanical Engineering, Qinghai University, Xining 810016, China

[d] Key Laboratory of Automobile Materials of Ministry of Education & School of Materials Science and Engineering, Nanling Campus, Jilin University, Changchun 130025, China

[e]State Key Laboratory of Metal Matrix Composites, Shanghai Jiao Tong University, Shanghai 200240, China

* Corresponding author: xqzeng@sjtu.edu.cn and yanjun.li@ntnu.no

Abstract

In this study, an *in situ* SEM/EBSD study on slip-induced extension twinning (S→T) behaviors of a Mg–Y alloy was conducted. It shows that the S→T process cannot be well explained using the classical geometrical compatibility parameter (m') determined by macroscopic stress. A new experimental method is proposed to unequivocally determine the slip directions of the source slip systems by combining the lattice rotation analysis and the slip trace analysis. By using the experimentally determined active slip systems, the validity of m' to reveal the S→T mechanism is improved. By a detailed study on lattice rotations of the grains containing source slip for twinning, it is found that the S→T process is dominated by micro deformation instead of macro deformation. This study emphasizes the importance of considering the effect of microscopic deformation when attempting to understand the S→T process in deformed magnesium alloys.

Keywords

Magnesium alloy; micro deformation; slip-induced twinning; lattice rotation; geometrical compatibility; EBSD

1. Introduction

It is well known that grain boundaries (GBs) have strong influences on the strength and plastic deformation behaviors of polycrystalline materials (Wang et al., 2014b; Lentz et al., 2015; Cepeda-Jiménez et al., 2015; Sangid et al., 2011; Lim et al., 2011). GBs have the influence of impeding dislocation movements from one grain to its adjacent grains. Therefore, dislocations will pile up in front of GBs during plastic deformation, causing sharp increases in local stress. As localized stress concentration exceeds certain critical levels, dislocation slip can be activated in the neighbor grains (so-called slip transfer) to balance the heterogeneous stress distribution and avoid premature fractures during tension and compression deformation (Bieler et al., 2009, 2019; Bayerschen et al., 2016; Kacher et al., 2014; Guo et al., 2014).

For metals with low stacking fault energy, in addition to dislocation slip, deformation twins can also be activated in the neighbor gains. This is so called slip-induced twinning (S→T), which is considered as another important deformation mechanism to maintain local deformation compatibility (Reddy et al., 2019; Kumar et al., 2017; Wang et al., 2010; Lind et al., 2014; Beyerlein et al., 2010, 2012). In magnesium (Mg) alloys, profuse basal <a> dislocations can pile up in front of GBs and subsequently lead to a stress concentration at GBs. To relieve the stress concentration, nucleation of extension twins in adjacent grains is often triggered (Guan et al., 2019; Chelladurai et al., 2019; Khosravani et al., 2013, 2015; Wang et al., 2014a; Liu et al., 2016b). For instance, Khosravani et al. (2015) showed high density of <a> geometrically necessary dislocations (GNDs) in the vicinity of GBs in the grains neighboring to the extension twin nucleation sites in a deformed Mg–3Al–1Zn alloy. Recent studies on HCP metals show that such type of extension twinning mostly occurs at GBs with misorientation angles of 30°−65° and does not necessarily follow the Schmid criterion, as most observed extension twin variants are not the one with the highest Schmid factor (SF) among the six possible $\{10\bar{1}2\}$ twin variants (Guan et al., 2019; Khosravani et al., 2015; Wang et al., 2014a; Liu et al., 2016b). The slip-induced twinning behavior has been explained by using the geometrical compatibility parameter, m' (Luster and Morris, 1995; Wang et al., 2010):

$$m' = \cos\psi \cdot \cos\kappa = (\boldsymbol{n}^{s} \cdot \boldsymbol{n}^{t}) \cdot (\boldsymbol{b}^{s} \cdot \boldsymbol{b}^{t}) \quad (1)$$

where ψ is the angle between the source slip plane normal ($\boldsymbol{n}^{s}$) and the activated twin plane normal ($\boldsymbol{n}^{t}$) and κ is the angle between the source dislocation slip direction ($\boldsymbol{b}^{s}$) and the twin shear direction ($\boldsymbol{b}^{t}$). When there is a good geometrical alignment between the source dislocation slip and a possible extension twin variant, namely a high m' (Guan et al., 2019; Wang et al., 2010; Bieler et al., 2014), the corresponding twin variant is likely to be triggered. Experimentally, the slip plane of the source dislocation system of S→T is usually determined by surface traces of dislocation slip, while the corresponding slip direction is often assumed to be the slip direction with the highest SF with regards to the global deformation stress (Guan et al., 2019; Wang et al., 2010; Liu et al., 2016b; Wang et al., 2014a). It has been shown by many research works that m' can be well applied to interpret S→T processes (Wang et al., 2010; Guan et al., 2019; Bieler et al., 2014). However, it is known that deformation in polycrystalline metals and alloys is usually heterogeneous at microstructural scale because of plastic anisotropy (Agnew et al., 2018; Orozco-Caballero et al., 2017; Liu et al., 2018). As a result, local deformation states in grains are not always controlled by the macro deformation stress. So, a question is raised: does the S→T process follow the macro stress or micro stress?

Up to now, most of the experimental studies on dislocation activities were based on transmission electron microscopy (TEM) (Wang et al., 2019; Sandlöbes et al., 2012, 2013; Zhang et al., 2016). It is easy to determine the types of dislocations existing in a deformed grain using the $\boldsymbol{g}\cdot\boldsymbol{b}$ criterion (Sandlöbes et al., 2013; Zhang et al., 2016), where $\boldsymbol{g}$ is diffraction vector and $\boldsymbol{b}$ is Burgers vector of dislocation, however, it is difficult to gain a statistical correlation between the dislocation activities and the macro deformation. Recently, the synchrotron-based X-ray microdiffraction (μXRD) technique has been used to analyze the dislocation activities by using Laue patterns, which often display streaked peaks because of the existence of GNDs that distort the local lattice (Zhou et al., 2019; Zhang et al., 2018; Li et al., 2018). This technique can be used to identify the slip systems of GNDs by simulating the streak directions of the diffraction peaks in a Laue pattern, but it is time-consuming. Alternatively, one can

analyze dislocation activities according to surface slip traces from a great number of grains with crystal orientations determined by electron backscattered diffraction (EBSD) (Bieler et al., 2019; Wang et al., 2010; Boehlert et al., 2012; Wang et al., 2016; Cepeda-Jiménez et al., 2015; Wang et al., 2014a; Zhu et al., 2019). However, it is difficult to determine the exact Burgers vectors of active dislocations by this method. For example, an observed (0001) basal slip trace can be caused by the dislocations with Burgers vector $[\bar{1}\bar{1}20]$, $[2\bar{1}\bar{1}0]$, and/or$[\bar{1}2\bar{1}0]$. We cannot obtain the exact Burgers vector(s) of the observed basal slip trace, as the EBSD-based slip trace analysis just offers the information of the basal slip plane (Xu et al., 2019).

This work aims to study the S→T behavior in a polycrystalline Mg–Y alloy by *in situ* SEM/EBSD. A new method to identify slip systems was developed based on the local lattice rotation in EBSD images. The m' values determined by macroscopic stress and the ones determined by the actual source slip system were compared. It shows that m' turns to be more rational to interpret the S→T process as the real source slip systems are adopted. The facts that affect the usage of m' were discussed as well.

2. Experimental procedure

The material used in the present work was a binary Mg–5 wt.% Y cast ingot, which was prepared by using commercial purity Mg (99.95 wt.%) and a Mg–25 wt.% Y master alloy by electric resistance melting in a steel crucible under a cover gas mixed of SF_6 (1 vol.%) and CO_2 (99 vol.%) at 1003 K. The liquid metal was stirred for 5 minutes and then kept for 15 minutes at the same temperature to ensure a homogeneous composition before pouring into a steel mold preheated to 423 K. The chemical composition of the obtained ingot was measured by inductively coupled plasma atomic emission spectroscopy (ICP). The billets were solution treated at 813 K for 24 h, extruded at 773 K (extrusion ratio = 18:1), and finally annealed at 803 K for 15 min.

Sheet samples for *in situ* tensile tests with nominal gauge dimensions of 11 mm × 4 mm × 1.4 mm (Length × Width × Thickness) were fabricated by electron discharge machining from the extruded rod, with the tensile axis being parallel to the extrusion

direction (ED). One surface of the samples was electro-polished in an ethanol solution containing 10 vol.% perchloric acid at 30 V and 243 K for 150 s. *In situ* room temperature tensile experiment was employed in a scanning electron microscope (ZEISS, Merlin compact) equipped with an EBSD detector (Oxford, NordlysMax^2) and a commercial testing module (Deben, Microtester 2 kN). The initial strain rate is 6.0×10^{-4} s^{-1} (the constant tensile speed of 0.4 mm/min). *In situ* SEM was used to track the evolution of microstructures at tensile strains of 0%, 2.5%, 5.0%, and 10.0%. After the SEM imaging, the corresponding orientation data of grains were obtained to further analyze the types of activated extension twins and intragranular orientation gradient. To optimize the quality of imaging and the acquisition time, an operating voltage of 20 kV and scanning step sizes of 0.5 and 1.0 μm were applied for EBSD data collection.

3. Results

3.1 Texture evolution and tensile behavior

The orientation evolution of grains in the Mg–5 wt.% Y sample during tensile deformation is presented by inverse pole figure (IPF) maps shown in Fig. 1. As can be seen, the initial microstructure has an average grain size of 96 μm (Fig. 1a). The corresponding {0001} pole figure is exhibited in the right. Because of the addition of Y, the maximum intensity of the texture component is 6.3 mrd, which is significantly lower than some extruded Y-free Mg alloys (Nakata et al., 2019; Zhao et al., 2019). The microstructure and texture of the sample at 2.5% and 5.0% tensile strain are provided in Figs. 1b and 1c, respectively. The maximum intensity of the texture component at 5.0% tensile strain was slightly increased to 6.7 mrd. Fig. 1d shows that only a small fraction (~1.0% in area fraction) of twins exist in the sample at 10.0% tensile strain. Totally, 13 S→T cases were identified in the region of interest (900 μm × 1140 μm) in the tensile sample. Two representative regions enclosed by black rectangles (Regions 1 and 2 in Fig. 1d) will be used for further analysis of the S→T processes. The engineering strain-stress curve of the *in situ* test is plotted in Fig. 1e. The stress drops due to the stress relaxation occurring when the tests were paused for EBSD and SEM

imaging. The Mg–Y alloy shows an impressive tensile strain of 25.0%.

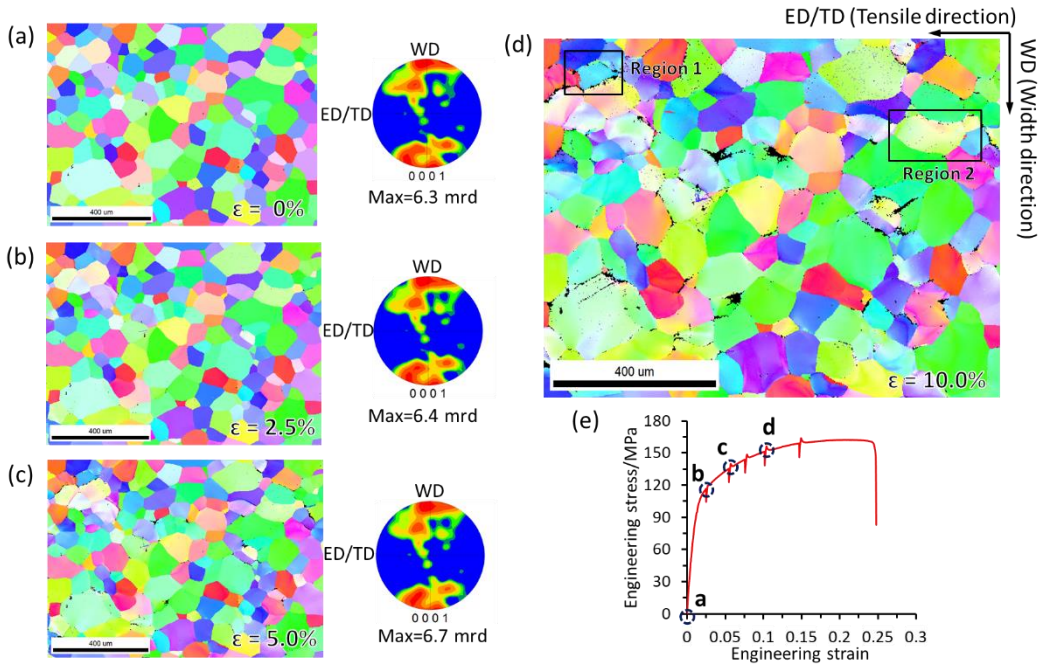

Fig. 1. *In situ* EBSD results showing the microstructure evolution of the Mg–Y sample during the tensile test at room temperature. (a) is the IPF map of the initial microstructure, and the initial texture in the form of {0001} pole figure is displayed in the right; (b), (c), and (d) are the IPF maps of the microstructure at 2.5%, 5.0%, and 10.0% strain, respectively; (e) is the engineering strain-stress curve of the *in situ* tensile test.

3.2 Observation on S→T processes

Fig. 2 shows a representative S→T process (Region 2 in Fig. 1d) where the source dislocation slip in grain G1 (average Euler angles = (252°, 61°, 320°)) and the triggered twin in grain G2 (average Euler angles = (256°, 102°, 9°)) are recorded. Figs. 2a–d show the orientation evolution of G1, G2, and surrounding grains. When the tensile strain reaches 10.0% (Fig. 2d), the middle-upper region in grain G1 changes to weak pink color, showing a good example of local deformation at sub-grain level.

The SEM image (Fig. 2e) shows that some sparse slip bands have emerged in grain G1 at 2.5% tensile strain. Based on the grain orientation data from EBSD, it can be

determined that the planar slip bands are aligned with the traces of (0001) basal planes, implying the activities of basal dislocations. As the strain reaches 5.0% (Fig. 2f), the spacing of slip lines in grain G1 becomes smaller, indicating more basal dislocation slip activities. In grain G2, tiny twins have formed at the GB between grains G1 and G2. These twins have a sword shape, thicker at the GB and with a tip pointing the interior of grain G2, confirming that these deformation twins have nucleated at the grain boundary and then grown into grain G2. At 10.0% tensile strain, a further growth of the twins can be observed (Fig. 2g).

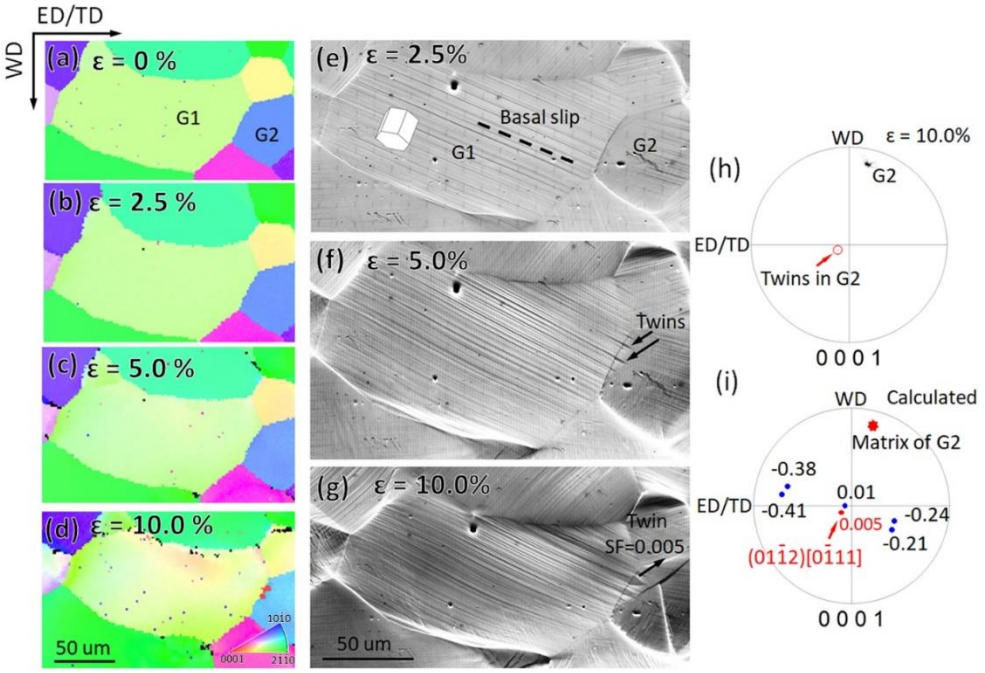

Fig. 2. *In situ* investigation of the S→T process and type identification of the triggered extension twin variant. (a)–(d) are the IPF maps at 0%, 2.5%, 5.0%, and 10.0% tensile strain, respectively; (e)–(g) are the SEM images at 2.5%, 5.0%, and 10.0% strain, respectively. (h) shows the {0001} pole figure of grain G2 and the triggered twin at 10.0% tensile strain; (i) shows the calculated {0001} pole figure of grain G2 and its six possible twin variants with corresponding SFs. It is worth mentioning that the extension twins appearing at 5.0% strain are too small to be recorded by EBSD scanning, while it is successful to obtain their orientation information at 10.0% strain because the twins have grown into a thickness comparable to the EBSD scan step (1.0 μm).

Fig. 2h shows the {0001} pole figure of grain G2 and the induced twins. Fig. 2i shows the {0001} poles of all the six possible $\{10\bar{1}2\}$ extension twin variants of grain G2. The calculated SFs corresponding to each twin variant are also labeled in the figure. The activated twin system in grain G2 is identified to be $(01\bar{1}2)[0\bar{1}11]$ based on the comparison between Figs. 2h and 2i.

The SFs of 3 basal dislocation slip systems in grain G1 have been calculated according to the macro tensile stress. The basal slip system $(0001)[\bar{1}\bar{1}20]$ is supposed to be activated, as its SF (0.26) is higher than the other two basal slip systems $(0001)[2\bar{1}\bar{1}0]$ and $(0001)[\bar{1}2\bar{1}0]$, with SF values of 0.17 and 0.085, respectively.

Table 1 lists the calculated SFs of the extension twin variants in grain G2 and the calculated ψ, κ, and m' with respect to the basal slip system $(0001)[\bar{1}\bar{1}20]$. As can be seen, the activated twin variant in grain G2 has a near-zero SF (0.005), showing that the activation of the twining system was not caused by the macro tensile stress but induced by the dislocation slip in grain G1. However, the calculated m' value of this activated twin variant is only 0.197, much lower than one of the other twin variants (0.618). It indicates that the m' criterion cannot be used to predict the twin variant selection in this S→T case.

Table 1. Geometric analysis of grain G2's six extension twin variants with respect to the $(0001)[\bar{1}\bar{1}20]$ basal slip in grain G1.

Twin variants	SF	ψ(°)	κ(°)	m'
$(10\bar{1}2)[\bar{1}011]$	-0.21	37	39	0.618
$(01\bar{1}2)[0\bar{1}11]$*	0.005	3	79	0.197
$(\bar{1}102)[1\bar{1}01]$	-0.41	42	118	-0.350
$(\bar{1}012)[10\bar{1}1]$	-0.24	72	124	-0.166
$(0\bar{1}12)[01\bar{1}1]$	0.01	84	89	0.002
$(1\bar{1}02)[\bar{1}101]$	-0.38	70	47	0.240

* Operating twin system

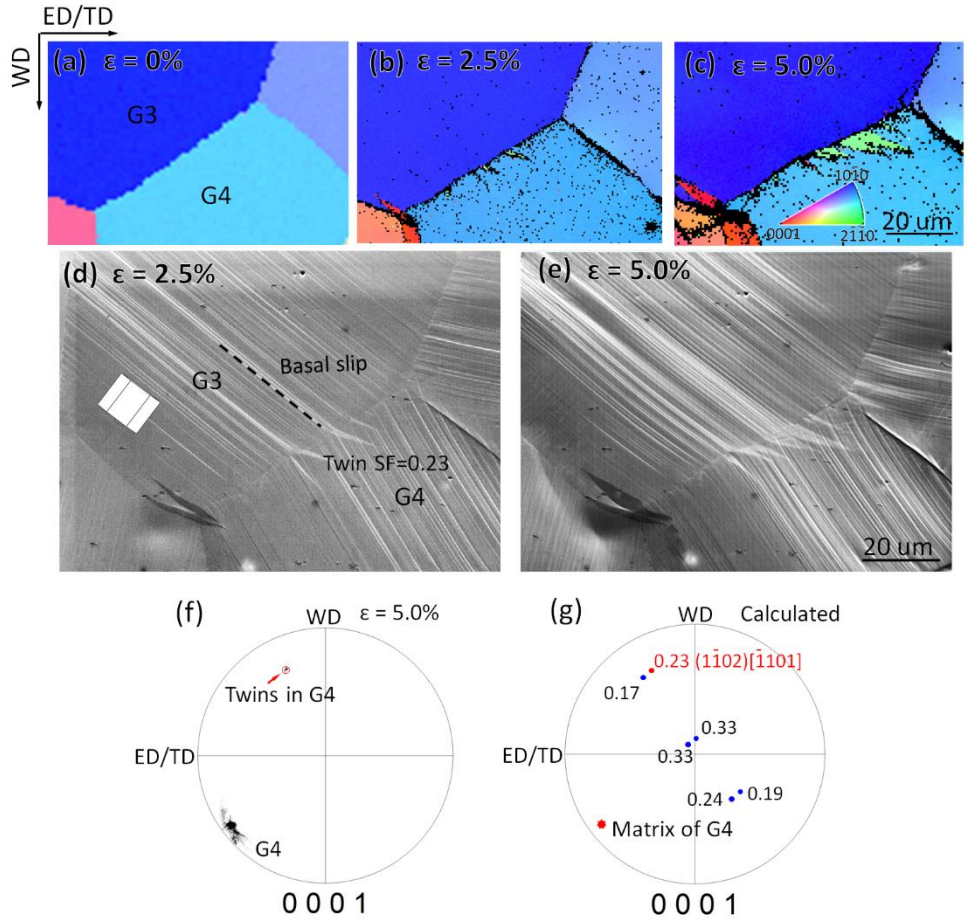

Fig. 3. *In situ* investigation of the second S→T case. (a)–(c) are the IPF maps at 0%, 2.5%, and 5.0% tensile strain, respectively; (d) and (e) are the SEM images at 2.5% and 5.0% strain, respectively; (f) shows the {0001} pole figure of grain G4 and the triggered twin at 5.0% tensile strain; (g) shows the calculated {0001} pole figure of grain G4 and its six possible twin variants with corresponding SFs.

Fig. 3 shows another S→T case (Region 1 in Fig. 1d**)**. As shown in Fig. 3d, basal slip in grain G3 (average Euler angles = (236°, 94°, 359°)) has stimulated the twins in grain G4 (average Euler angles = (215°, 85°, 10°)) at 2.5% strain. The SF values of basal slip systems $(0001)[2\bar{1}\bar{1}0]$, $(0001)[\bar{1}2\bar{1}0]$, and $(0001)[\bar{1}\bar{1}20]$ in grain G3 are calculated as 0.46, 0.24, and 0.22, respectively. It is therefore supposed that $(0001)[2\bar{1}\bar{1}0]$ is the activated dominant source dislocation slip. The activated twin system in grain G4 is identified as $(1\bar{1}02)[\bar{1}101]$ by the comparison between Figs. 3f and 3g. Table 2 compares SFs of all the six extension twin variants in grain G4 and the

calculated ψ, κ, and m' with respect to the $(0001)[2\bar{1}\bar{1}0]$ basal slip in grain G3. The activated twin system also has a small SF (0.23), ranked No. 4 among all the twin variants, confirming that the twinning is not caused by the macro tensile stress. However, a high m' value of 0.828 was calculated for the experimentally determined twin variant. In this case, the m' criterion can be well applied to explain the S→T mechanism.

Table 2. Geometric analysis of grain G4's six extension twin variants with respect to the $(0001)[2\bar{1}\bar{1}0]$ basal slip in grain G3.

Twin variants	SF	ψ(°)	κ(°)	m'
$(10\bar{1}2)[\bar{1}011]$	0.24	37	39	0.615
$(01\bar{1}2)[0\bar{1}11]$	0.33	58	82	0.073
$(\bar{1}102)[1\bar{1}01]$	0.17	66	113	-0.160
$(\bar{1}012)[10\bar{1}1]$	0.19	57	106	-0.156
$(0\bar{1}12)[01\bar{1}1]$	0.33	35	69	0.289
$(1\bar{1}02)[\bar{1}101]$*	0.23	20	28	0.828

* Operating twin system

To further evaluate the validity of the m' criterion, the same analysis is performed on all the rest S→T cases and the m' values determined by the macroscopic deformation are shown in Fig. 4. The observed S→T events are labeled as T1–T13. A careful analysis shows that, for 5 of the 13 cases, the activated twin variants do not have the highest m' value, implying that the m' value determined by the macroscopic deformation is not sufficient to predict the twin variant during these S→T processes. As shown in Fig. 4, the 5 S→T cases have m' values lower than 0.5.

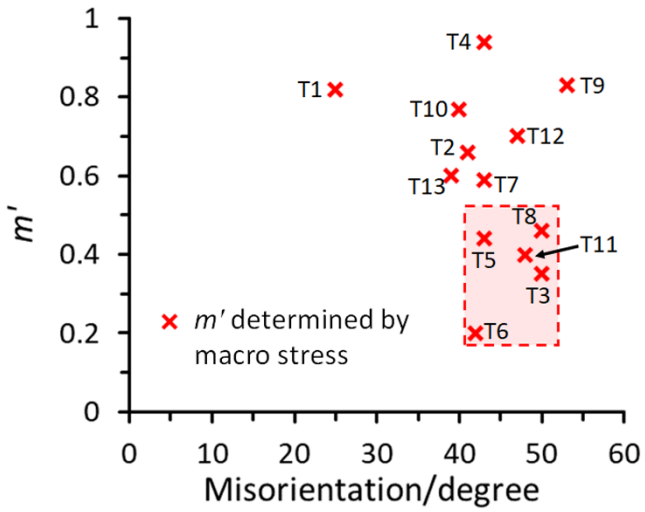

Fig. 4. m' parameter of 13 observed S→T cases calculated using the source slip system determined by the macroscopic stress, as a function of misorientation angle of GB. The S→T cases with m' less than 0.5 are framed by the red shaded box.

3.3 Analysis of the local deformation mechanism for S→T processes

To explore the reason why a large fraction of the S→T cases do not follow the m' criterion, the local deformation behaviors of the grains containing source dislocation slip have been investigated. It is well known that, as a result of basal <a> dislocation slip, the slip direction of crystal will turn to align with the tensile direction while the *c*-axis of crystal will turn to the direction perpendicular to the tensile direction. It means, when the deformation of grains is dominated by macro stress, the (0001) pole of grains will rotate towards width direction (WD) or normal direction (ND) (Mayama et al., 2009).

Figs. 5a and 5b show composite $\{0001\}$ and $\{11\bar{2}0\}$ pole figures of grain G1 subjected to two different tensile strains (0% and 5.0%), respectively. From the composite pole figures, the trajectory of the lattice rotation during deformation can be tracked. As can be seen in Fig. 5a, the (0001) pole has gradually moved downwards, instead of towards WD or ND directions according to the macro tensile strain during tensile deformation. Also, in the $\{11\bar{2}0\}$ pole figure (Fig. 5b), the projected spots do not show obvious rotations to the ED/TD direction. The $(\bar{1}\bar{1}20)$ pole, i.e. the slip direction of the supposed basal slip system according to the largest SF, even rotates

away from ED/TD, which indicates that the deformation of grain G1 has not followed the macro tensile strain.

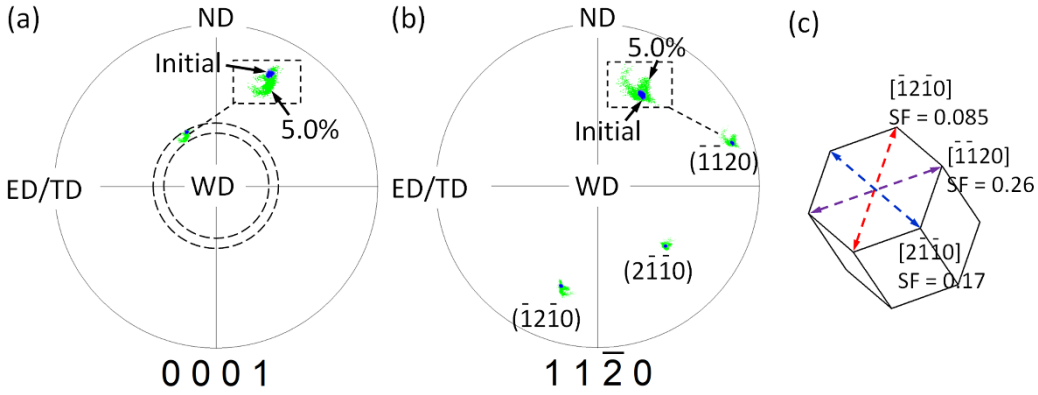

Fig. 5. Deformation state analysis on grain G1 based on the movement trajectory of the projected spot in the {0001} and {11$\bar{2}$0} pole figure. (a) and (b) are the {0001} and {11$\bar{2}$0} pole figure of grain G1, respectively. (c) is the crystal lattice of grain G1 projected on the ED/TD–ND plane. The basal slip directions with corresponding SFs are indexed as well. For interpretation of the references to color in this figure legend, the reader is referred to the web version of this article.

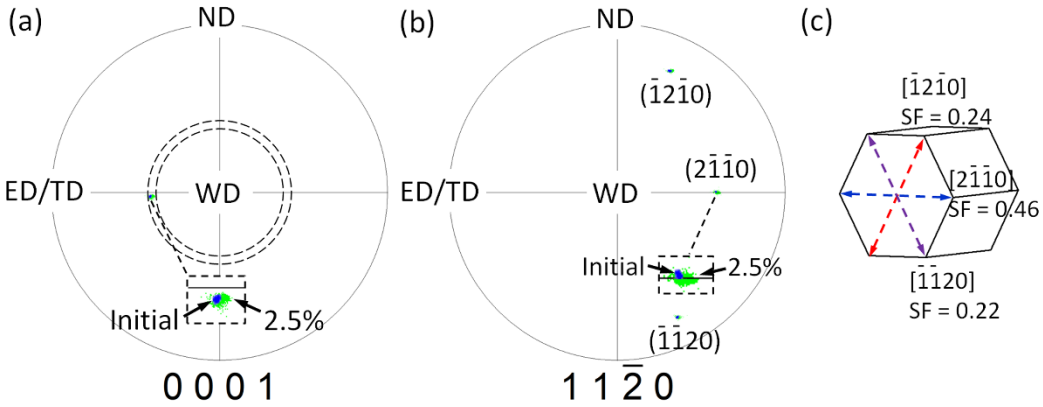

Fig. 6. Deformation state analysis on grain G3 based on the movement trajectory of the projected spot in the {0001} and {11$\bar{2}$0} pole figure. (a) and (b) are the {0001} and {11$\bar{2}$0} pole figure of grain G3, respectively. (c) is the crystal lattice of grain G3 projected on the ED/TD–ND plane. The basal slip directions with corresponding SFs are indexed as well. For interpretation of the references to color in this figure legend, the reader is referred to the web version of this article.

A similar analysis was conducted on grain G3 as well. As can be seen in the enlarged rotation trajectory in Fig. 6a, the (0001) pole of grain G3 shows a streak extending to the center of the pole figure at 2.5% tensile strain, indicating that the *c*-axis of grain G3 rotates towards the WD direction. It can be observed from Fig. 6b that $(2\bar{1}\bar{1}0)$ pole is rotating to the ED/TD direction simultaneously, showing that $[2\bar{1}\bar{1}0]$ direction of the crystal lattice rotates towards ED/TD direction. This confirms that the basal $[2\bar{1}\bar{1}0]$ dislocation slip in grain G3 has been activated by the macro tensile stress.

Table 3. Schmid factors of dislocation slips in the S→T cases and dominating deformation mechanism.

	$SF_{Basal\ slip}$			Dominating deformation mechanism
	$(0001)[2\bar{1}\bar{1}0]$	$(0001)[\bar{1}2\bar{1}0]$	$(0001)[\bar{1}\bar{1}20]$	
Case T1	0.46*	0.24	0.22	Macro
Case T2	0.19	0.18	0.37*	Macro
Case T3	0.13*	0.25	0.12	**Micro**
Case T4	0.08*	0.07	0.009	Macro
Case T5	0.15	0.11*	0.04	**Micro**
Case T6	0.17	0.085*	0.26	**Micro**
Case T7	0.41*	0.09	0.32	Macro
Case T8	0.06	0.39	0.33*	**Micro**
Case T9	0.47*	0.25	0.22	Macro
Case T10	0.19	0.34*	0.15	Macro
Case T11	0.27	0.19	0.46*	Macro
Case T12	0.13	0.43*	0.30	Macro
Case T13	0.04*	0.006	0.05	**Micro**

* Source slip system

The deformation states of the grains with source dislocation slip in all the S→T cases were examined using the same approach, and the results are listed in Table 3. It shows that the dislocation slip in 8 grains is controlled by the macro deformation and their dominating slip systems can be determined by the Schmid criterion. In contrast, for the rest 5 S→T cases, the source dislocation slip does not follow the macro tensile stress. Therefore, the Schmid criterion cannot be used to identify the real source dislocation slip. This explains why the *m'* criterion does not work for these cases.

3.4 Determination of the real source slip system for S→T processes

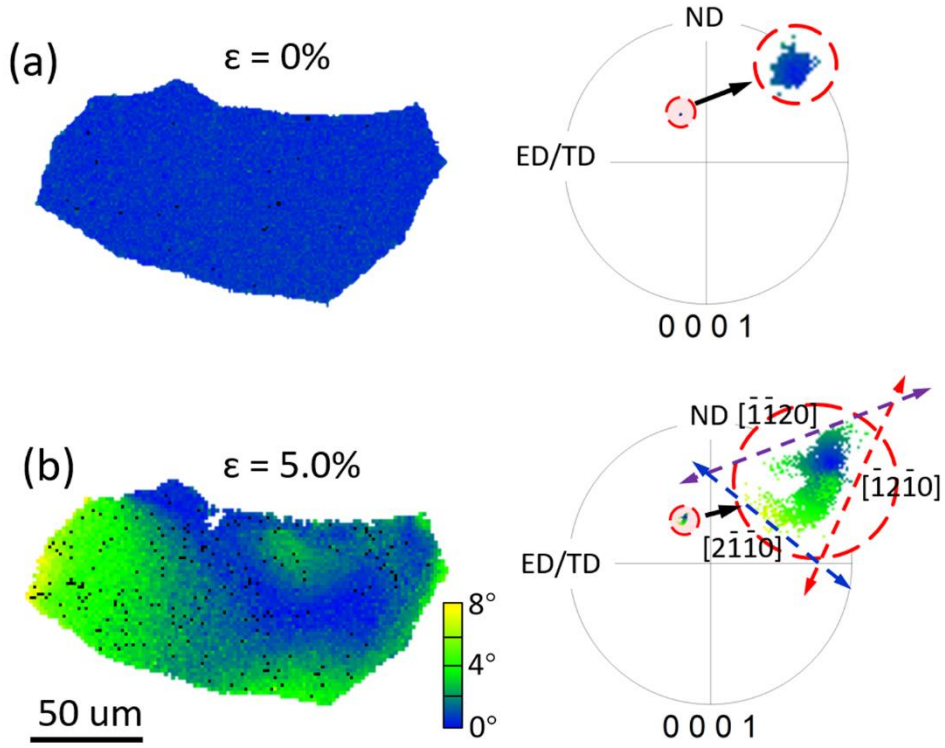

Fig. 7. The evolution of orientation gradient and shape of the (0001) pole during the tensile deformation of grain G1. (a) and (b) are the orientation gradient maps and corresponding {0001} pole figures of grain G1 at 0% and 5.0% tensile strain, respectively. For interpretation of the references to color in this figure legend, the reader is referred to the web version of this article.

The real source basal slip systems in those grains, which do not follow the macro tensile deformation, can be identified by examining the moving trajectory of the (0001)

poles. Fig. 7a gives the orientation gradient map and the corresponding {0001} pole figure of grain G1 before tensile deformation. It shows that no obvious misorientation exists in grain G1 before deformation. As the tensile strain reaches 5.0% (Fig. 7b), clear orientation gradient appears in grain G1. Apart from a main streak direction along $[\bar{1}2\bar{1}0]$, the spot of (0001) pole is stretched along the directions of $[\bar{1}\bar{1}20]$ and $[2\bar{1}\bar{1}0]$ of the projected crystal lattice of grain G1 as well (compare the blue and purple arrows in Fig.7b and Fig. 5c), showing that dislocation slip has caused local lattice rotation in the grain.

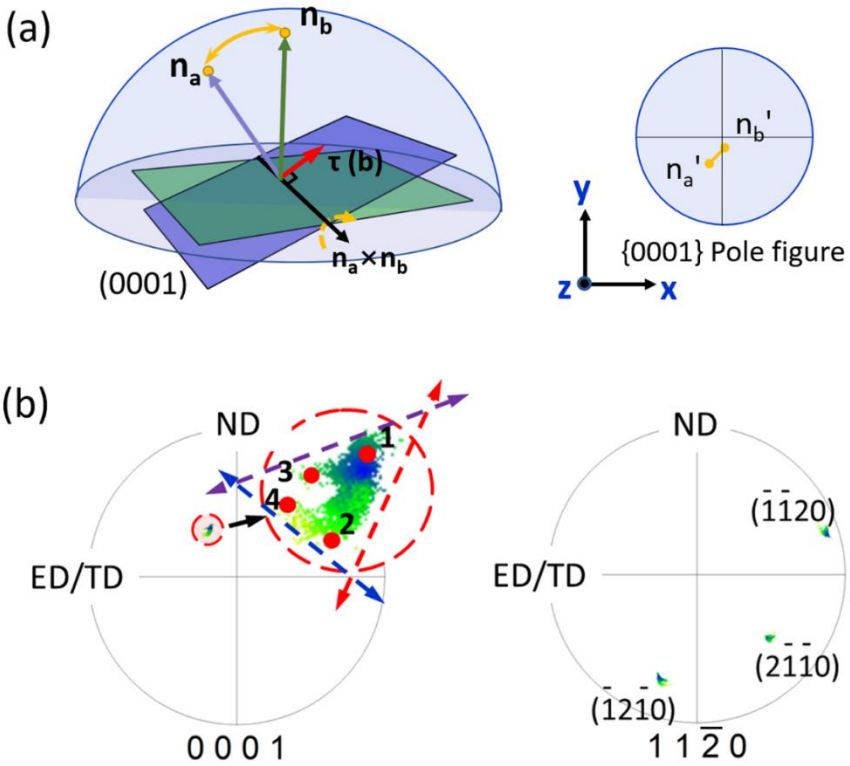

Fig. 8. The relationship between the types of basal <a> slip and the streaked directions of the spot in the {0001} pole figure. (a) is the schematic illustration for a lattice rotation mechanism during deformation, where $\boldsymbol{\tau}$ ($\boldsymbol{b}$), $\boldsymbol{n}_a$, and $\boldsymbol{n}_b$ are the resolved shear stress (the corresponding Burgers vector), the initial vector of *c*-axis, and the vector of *c*-axis after lattice rotation, respectively. n_a' and n_b' are the projected points of the $\boldsymbol{n}_a$ and $\boldsymbol{n}_b$ on the{0001} pole figure. (b) shows the {0001} and $\{11\bar{2}0\}$ pole figure of grain G1. Based on the two-dimensional coordinates in the {0001} pole figure, the space coordinates of the nodes (1, 2, 3, and 4) can be obtained. Based on the $\{11\bar{2}0\}$ pole figure, the space vectors of the basal <a> slip directions can be obtained.

During basal <a> dislocation slip in HCP materials, the rotation axis of crystal will be perpendicular to the corresponding Burgers vector and the normal of slip plane (Jia et al., 2019; Jin et al., 2016). Fig. 8a shows this rotation mechanism of basal plane. Because of the basal plane's rotation, its original *c*-axis $\boldsymbol{n}_a$ moves to $\boldsymbol{n}_b$. It is not hard to imagine that there is a streak along the orange line connected by n_a' and n_b' in the {0001} pole figure. Depending on the coordinates of n_a' and n_b', the space vectors of $\boldsymbol{n}_a$ and $\boldsymbol{n}_b$ can be reconstructed. Thus, we can deduce the exact slip direction by the relationship that the Burgers vector of the slip system ($\boldsymbol{b}$) is perpendicular to the rotation axis ($\boldsymbol{n}_a \times \boldsymbol{n}_b$).

Using the relationship above, the dominating basal <a> dislocation in grain G1 can be identified. The reconstructed space coordinates of points 1, 2, 3, and 4 in Fig. 8b are $\boldsymbol{n}_1$ (-0.258, 0.506, -0.823), $\boldsymbol{n}_2$ (-0.301, 0.400, -0.866), $\boldsymbol{n}_3$ (-0.334, 0.477, -0.813), and $\boldsymbol{n}_4$ (-0.364, 0.445, -0.818), respectively. The space vectors of basal <a> slip direction $[\bar{1}\bar{1}20]$, $[2\bar{1}\bar{1}0]$, and $[\bar{1}2\bar{1}0]$ are $\boldsymbol{b}_1$ (0.941, 0.311, -0.131), $\boldsymbol{b}_2$ (0.634, -0.564, -0.528), and $\boldsymbol{b}_3$ (-0.312, -0.867, -0.388), respectively. Each of the above space coordinates and vectors was an average based on five measurements for each of the tips and poles in Fig. 8b. The results of the vector operation ($\boldsymbol{b}_3 \cdot (\boldsymbol{n}_1 \times \boldsymbol{n}_2) \sim$ -0.05) show that the $[\bar{1}2\bar{1}0]$ ($\boldsymbol{b}_3$) is almost perpendicular to the rotation axis $\boldsymbol{n}_1 \times \boldsymbol{n}_2$ reconstructed by space coordinates of nodes 1 and 2, which indicates that the lattice rotation from 1 to 2 is caused by the activity of the basal <a> slip system with Burgers vector $[\bar{1}2\bar{1}0]$. The results of the vector operation ($\boldsymbol{b}_2 \cdot (\boldsymbol{n}_2 \times \boldsymbol{n}_4) \sim$ -0.09) show that the $[2\bar{1}\bar{1}0]$ ($\boldsymbol{b}_2$) is almost perpendicular to the rotation axis $\boldsymbol{n}_2 \times \boldsymbol{n}_4$, which indicates that the streak direction from 2 to 4 is caused by the activity of the basal <a> slip system with Burgers vector $[2\bar{1}\bar{1}0]$. Again, the $[\bar{1}\bar{1}20]$ ($\boldsymbol{b}_1$) is almost perpendicular to the rotation axis $\boldsymbol{n}_1 \times \boldsymbol{n}_3$ ($\boldsymbol{b}_1 \cdot (\boldsymbol{n}_1 \times \boldsymbol{n}_3) \sim$ -0.04), which indicates that the streak direction from 1 to 3 is caused by the activity of the basal <a> slip system with Burgers vector $[\bar{1}\bar{1}20]$. From the stretching extent of the projected spot, it can be concluded that the deformation in grain G1 is dominated by $(0001)[\bar{1}2\bar{1}0]$.

The dominating source dislocation slip systems of all the S→T cases dominated by micro deformation mechanism have been obtained by this method and the results

are listed in Table 3 as well.

3.5 *m′* values corrected by real dislocation slip

After identifying the source slip systems of all the S→T cases by considering the effect of micro deformation on the S→T behavior, the *m′* parameters were recalculated based on the real basal slip systems. As an example, Table 4 shows the recalculated κ and *m′* with respect to the basal slip $(0001)[\bar{1}2\bar{1}0]$ in grain G1. It can be seen that the values of κ are quite different from the values in Table 1. Now, the activated twin variant in grain G2 has the highest *m′* value of 0.946. Fig. 9 represents the new *m′* values by using the real source slip systems identified by the new method. It is clear that the *m′* parameters for 4 of the 5 cases framed by red shaded box in Fig. 4 have been much increased. With the corrected *m′* values, the twin variant selection in 12 of the 13 S→T cases can be predicted by using the *m′* criterion.

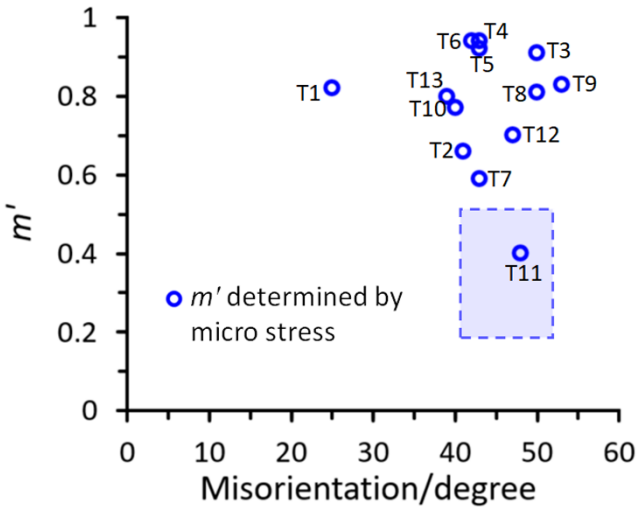

Fig. 9. Distribution of the *m′* parameter with respect to the real source slip system, as a function of misorientation angle of GB. The area framed by the blue shaded box is corresponding to the area framed by the red shaded box in Fig. 4.

Table 4. Geometric analysis based on the basal slip system $(0001)[\bar{1}2\bar{1}0]$ identified by lattice rotation analysis. The result shows that there is a good geometric relationship between the incoming slip system in grain G1 and the triggered twin variant in grain G2.

Twin variants	SF	ψ(°)	κ(°)	m'
$(10\bar{1}2)[\bar{1}011]$	-0.21	37	27	0.713
$(01\bar{1}2)[0\bar{1}11]$*	0.005	3	19	0.946
$(\bar{1}102)[1\bar{1}01]$	-0.41	42	61	0.365
$(\bar{1}012)[10\bar{1}1]$	-0.24	72	92	-0.008
$(0\bar{1}12)[01\bar{1}1]$	0.01	84	95	-0.008
$(1\bar{1}02)[\bar{1}101]$	-0.38	70	68	0.132

* Operating twin system

4. Discussion

The local deformation analysis in this work was based on the deformation features of the surface grains. It is known that the deformation of the grains in the free surface is less constrained by the surrounding grains and subjected to less back stress. It was revealed in a recent work (Wang et al., 2017) that the surface grains have a lower critical resolved shear stress (CRSS) for basal slip than that of the bulk grains in pure titanium, reflecting that the activation of dislocation slip may be slightly easier than that of the grains in the bulk of the aggregate. Moreover, a full-field crystal plasticity simulation has clearly shown that the overall strain distributions of the free surface and the entire volume of the sample are rather similar, though some strain differences exist (Martin et al., 2014). It indicates that the results obtained through the surface deformation features are representative to the deformation behavior of the entire volume of the bulk microstructure.

The m' criterion has been widely used to evaluate the S→T process. In many well-documented works (Guan et al., 2019; Wang et al., 2010; Bieler et al., 2014), the S→T

process can be well interpreted through the m' criterion. However, in this work, it shows that among all the 13 observed S→T cases, only 8 cases follow the m' criterion while the rest 5 show low m' twin variants. Such low m' value S→T cases have also been reported by other researchers (Liu et al., 2016b; Wang et al., 2014a). Although different possible reasons have been proposed, the mechanism behind was not clear. In this work, we have demonstrated that the slip activities of individual grains do not necessarily follow the macro deformation, namely the local stresses of grains can be largely different from the macro tensile stress, activating dislocation slip systems different from that determined by the Schmid factor criterion and therefore causing different twin variant selection of S→T processes. This experimental result is consistent with crystal plasticity finite element modeling (CPFEM) simulation results (Bieler et al., 2009; Martin et al., 2014; Kumar et al., 2017). The simulation work by Kumar et al. (2017) using a crystal plasticity model based on fast Fourier transforms (FFT) showed that the local stress around a deformation twin in a hcp crystal is strongly dependent of the neighboring grain orientations. The difference between local and macro strain has been observed by a digital image correlation (DIC) study combined with continuum crystal plasticity simulations on Mg alloys (Martin et al., 2014). It shown that no strong correlation exists between the magnitude of local strain in grains and Schmid factor. As discussed in the work by Bieler et al. (2009), the local deformation behavior in terms of slip activity will also influence the deformation compatibility at GB and accordingly the crack initiation. Our work further confirms the importance to take the micro deformation of grains into account when studying the deformation behaviors in polycrystalline materials.

It is shown in this work the real source dislocation slip can be identified by analyzing the lattice rotation of grains by using the moving trajectory of (0001) poles. The twin variant selection in 12 of the 13 S→T cases can be well interpreted by the high m' values (Fig. 9) obtained by adopting the experimentally determined source slip. Here, the good geometric compatibility (high m') ensures that the driving force from the grain with source dislocation slip is large enough to trigger the twins in the neighbor

grains. The validity of the m' criterion for interpretation of the twin variant selection of S→T processes is further confirmed.

However, it has to be mentioned that, even after recalculation of m' values, there is still one S→T case (T11 in Fig. 4) which cannot be well interpreted by the m' criterion. This may be ascribed to the complexity of the source dislocation activity at GBs. Here, we have only considered the basal dislocation slip. Due to the extremely high stress accumulated near GBs, dislocation slip systems with higher CRSS, such as prismatic <a> and pyramidal <a> dislocations, may also be activated, which can complicate the S→T process. Our very recent study reported that non-basal dislocations were occasionally observed near GBs (Zhou et al., 2019), which could cause the stress fluctuation and further affect the S→T process. Another reason can be ascribed to the simplified assumption for the S→T mechanism, where the activation of twin is only due to the source dislocation slip in a neighbor grain while the effects of other neighboring grains are not considered. In a very recent paper, Xin et al. (2019) studied twin-induced twin (i.e. T→T) processes using a composite Schmid factor (CSF), which incorporates both SF and m'. By using the CSF criterion, it is found that the twin variant selection of the S→T case T11 can be explained by CSF, but 2 other S→T events' twin variant selection become unexplained by CSF. It implies that S→T process may be affected by macroscopic stress to some extent, but cannot be thoroughly explained by simply introducing the SF effect (Guo et al., 2014). Furthermore, the orientation of GB plane may also affect the S→T process. The effects of GB plane have been considered in the slip-induced slip cases in some recent work (Sangid et al., 2011; Beyerlein et al., 2012). For instance, Beyerlein et al. (2012) pointed out that the formation of an efficient transmission pathway in the Cu/Nb bimetal interfaces depended on two geometrical factors: the angle between the Burgers vectors of a pair of fcc/bcc slip systems and the angle between the intersection lines that each slip plane makes with GB. Apparently, the angle between the lines of intersection at the GB plane can be changed by the orientation of GB plane, which may eventually affect the initiation of slip transfer. For the slip-induced twinning behavior in HCP metals, the influence of GB plane is not

known yet, which is worth of studying. Such an effect will be discussed in our ongoing work.

Besides the factors from micro deformation and the space structure of GB, the microchemistry and microstructure defect at GB could also affect the S→T process. Wang et al. (2000) reported simulation results that dislocation motion changes unexpectedly with variations in mean solute concentration. The strong solute segregation at GBs, as a very common phenomenon in Mg alloys (Nie et al., 2013; Liu et al., 2016a; Stanford et al., 2011), could lead to stress fluctuation when the mobile dislocations impinge GBs. The effect of GB microchemistry on the initiation of the S→T process and the selection of twin variants should be further studied, which can help to deepen the understanding of the S→T behavior in HCP polycrystals.

5. Conclusions

The S→T process in an extruded Mg–Y alloy was systematically investigated using *in situ* SEM/EBSD. The main results can be summarized as follows:

1. The m' values of 13 observed S→T cases were determined based on the slip trace analysis in SEM images, EBSD image analysis, and calculated Schmid factor. It shows that 5 of 13 S→T cases have m' less than 0.5, where the twin variant selection does not follow the m' criterion, indicating that the m' criterion determined by macroscopic stress is not sufficient to interpret the S→T process of these cases.
2. An evaluation of the deformation mechanism of the S→T cases was conducted based on the rotation trajectory of the poles in the {0001} and $\{11\bar{2}0\}$ pole figures. The results show that the activity of the source slip system in a large fraction of grains is controlled by micro deformation, which does not necessarily follow the macro deformation.
3. An experimental method was proposed to identify the real source slip systems for the S→T processes, i.e. by analyzing the lattice rotation of grains using the moving trajectory of {0001} poles during tensile deformation.
4. By using the real source dislocation slip systems determined by the new method,

the m' criterion is valid to interpret the twin variant selection of most (12 of 13) of the S→T cases, indicating that it is crucial to take into account the micro deformation when using the m' criterion to study the S→T process.

Acknowledgements

This work was financially supported by the National Natural Science Foundation of China (Nos. 51631006 and 51671127). The first author BJZ would like to express his gratitude to the China Scholarship Council (No. 201806230150).

Reference

Agnew, S.R., Singh, A., Calhoun, C.A., Mulay, R.P., Bhattacharyya, J.J., Somekawa, H., Mukai, T., Clausen, B., Wu, P.D., 2018. In-situ neutron diffraction of a quasicrystal-containing Mg alloy interpreted using a new polycrystal plasticity model of hardening due to {10.2} tensile twinning. Int. J. Plast. 100, 34–51.

Bayerschen, E., McBride, A.T., Reddy, B.D., Böhlke, T., 2016. Review on slip transmission criteria in experiments and crystal plasticity models. J. Mater. Sci. 51, 2243–2258.

Beyerlein, I.J., Capolungo, L., Marshall, P.E., McCabe, R.J., Tomé, C.N., 2010. Statistical analyses of deformation twinning in magnesium. Philos. Mag. 90, 2161–2190.

Beyerlein, I.J., Mara, N.A., Wang, J., Carpenter, J.S., Zheng, S.J., Han, W.Z., Zhang, R.F., Kang, K., Nizolek, T., Pollock, T.M., 2012, Structure–property–functionality of bimetal interfaces. JOM J. Miner. Metals Mater. Soc. 64, 1192–1207.

Bieler, T.R., Alizadeh, R., Peña-Ortega, M., Llorca, J., 2019. An analysis of (the lack of) slip transfer between near-cube oriented grains in pure Al. Int. J. Plast. 118, 269–290.

Bieler, T.R., Eisenlohr, P., Roters, F., Kumar, D., Mason, D.E., Crimp, M.A., Raabe, D., 2009. The role of heterogeneous deformation on damage nucleation at grain boundaries in single phase metals. Int. J. Plast. 25, 1655–1683.

Bieler, T.R., Eisenlohr, P., Zhang, C., Phukan, H.J., Crimp, M.A., 2014. Grain boundaries and interfaces in slip transfer. Curr. Opin. Solid St. M. 18, 212–226.

Boehlert, C.J., Chen, Z., Gutiérrez-Urrutia, I., Llorca, J., Pérez-Prado, M.T., 2012. In situ analysis of the tensile and tensile-creep deformation mechanisms in rolled AZ31. Acta Mater. 60, 1889–1904.

Cepeda-Jiménez, C.M., Molina-Aldareguia, J.M., Pérez-Prado, M.T., 2015. Effect of grain size on slip activity in pure magnesium polycrystals. Acta Mater. 84, 443–456.

Chelladurai, I., Adams, D., Fullwood, D.T., Miles, M.P., Niezgoda, S., Beyerlein, I.J., Knezevic, M., 2019. Modeling of trans-grain twin transmission in AZ31 via a neighborhood-based viscoplastic self-consistent model. Int. J. Plast. 117, 21–32.

Guan, D.K., Wynne, B., Gao, J.H., Huang, Y.H., Rainforth, W.M., 2019. Basal slip mediated tension twin variant selection in magnesium WE43 alloy. Acta Mater. 170, 1–14.
Guo, Y., Britton, T.B., Wilkinson, A.J., 2014. Slip band–grain boundary interactions in commercial-purity titanium. Acta Mater. 76, 1–12.
Jia, H., Marthinsen, K., Li, Y., 2019. Revealing abnormal {11-21} twins in commercial purity Ti subjected to split Hopkinson pressure bar. J. Alloys Comp. 783, 513–523.
Jin, S., Marthinsen, K., Li, Y., 2016. Formation of {11-21} twin boundaries in titanium by kinking mechanism through accumulative dislocation slip. Acta Mater. 120, 403–414.
Kacher, J., Eftink, B.P., Cui, B., Robertson, I.M., 2014. Dislocation interactions with grain boundaries. Curr. Opin. Solid St. M. 18, 227–243.
Khosravani, A., Fullwood, D.T., Adams, B.L., Rampton, T.M., Miles, M.P., Mishra, R.K., 2015. Nucleation and propagation of {10-12} twins in AZ31 magnesium alloy. Acta Mater. 100, 202–214.
Khosravani, A., Scott, J., Miles, M.P., Fullwood, D.T., Adams, B.L., Mishra, R.K., 2013. Twinning in magnesium alloy AZ31B under different strain paths at moderately elevated temperatures. Int. J. Plast. 45, 160–173.
Kumar, M.A., Beyerlein, I.J., Lebensohn, R.A., Tomé, C.N., 2017. Modeling the effect of neighboring grains on twin growth in HCP polycrystals. Model. Simulat. Mater. Sci. Eng. 25, 1–25.
Lentz, M., Klaus, M., Beyerlein, I.J., Zecevic, M., Reimers, W., Knezevic, M., 2015. In situ X-ray diffraction and crystal plasticity modeling of the deformation behavior of extruded Mg–Li–(Al) alloys: An uncommon tension–compression asymmetry. Acta Mater. 86, 254–268.
Li, R.G., Xie, Q.G., Wang, Y.D., Liu, W.J., Wang, M.G., Wu, G.L., Li, X.W., Zhang, M.H., Lu, Z.P., Geng, C., Zhu, T., 2018. Unraveling submicron-scale mechanical heterogeneity by three-dimensional X-ray microdiffraction. Proc. Natl. Acad. Sci. 115, 483–488.
Lim, H., Lee, M.G., Kim, J.H., Adams, B.L., Wagoner, R.H., 2011. Simulation of polycrystal deformation with grain and grain boundary effects. Int. J. Plast. 27, 1328–1354.
Lind, J., Li, S.F., Pokharel, R., Lienert, U., Rollett, A.D., Suter, R.M., 2014. Tensile twin nucleation events coupled to neighboring slip observed in three dimensions. Acta Mater. 76, 213–220.
Liu, C., Shanthraj, P., Diehl, M., Roters, F., Dong, S., Dong, J., Ding, W., Raabe, D., 2018. An integrated crystal plasticity–phase field model for spatially resolved twin nucleation, propagation, and growth in hexagonal materials. Int. J. Plast. 106, 203–227.
Liu, C.Q., Che, H.W., Nie, J.F., 2016a. Interphase boundary segregation of Zn in Mg–Sn–Zn alloys. Scr. Mater. 123, 5–8.
Liu, G.D., Xin, R.L., Shu, X.G., Wang, C.P., Liu, Q., 2016b. The mechanism of twinning activation and variant selection in magnesium alloys dominated by slip deformation. J. Alloys Comp. 687, 352–359.
Luster, J., Morris, J.M., 1995. Compatibility of deformation in two-phase Ti-Al alloys:

Dependence on microstructure and orientation relationships. Metall. Mater. Trans. A 26, 1745–1756.
Mayama, T., Aizawa, K., Tadano, Y., Kuroda, M., 2009. Influence of twinning deformation and lattice rotation on strength differential effect in polycrystalline pure magnesium with rolling texture. Comp. Mater. Sci. 47, 448–455.
Martin, G., Sinclair, C.W., Lebensohn, R.A., 2014. Microscale plastic strain heterogeneity in slip dominated deformation of a magnesium alloy containing rare-earth. Mater. Sci. Eng. A 603, 37–51.
Nakata, T., Bhattacharyya, J.J., Agnew, S.R., Kamado, S., 2019. Unexpected influence of prismatic plate-shaped precipitates on strengths and yield anisotropy in an extruded Mg–0.3Ca–1.0In–0.1Al–0.2Mn (at.%) alloy. Scr. Mater. 169, 70–75.
Nie, J.F., Zhu, Y.M., Liu, J.Z., Fang, X.Y., 2013. Periodic segregation of solute atoms in fully coherent twin boundaries. Science 340, 957–960.
Orozco-Caballero, A., Lunt, D., Robson, J.D., Fonseca, J.Q.D., 2017. How magnesium accommodates local deformation incompatibility: A high-resolution digital image correlation study. Acta Mater. 133, 367–379.
Reddy, G.B., Kapoor, R., Sarkar, A., 2019. Probability based ranking approach for twin variant selection in an α-Zr alloy. Int. J. Plast. 122, 164–167.
Sandlöbes, S., Friák, M., Neugebauer, J., Raabe, D., 2013. Basal and non-basal dislocation slip in Mg–Y. Mater. Sci. Eng. A 576, 61–68.
Sandlöbes, S., Friák, M., Zaefferer, S., Dick, A., Yi, S., Letzig, D., Pei, Z., Zhu, L.F., Neugebauer, J., Raabe, D., 2012. The relation between ductility and stacking fault energies in Mg and Mg–Y alloys. Acta Mater. 60, 3011–3021.
Sangid, M.D., Maier, H.J., Sehitoglu, H., 2011. The role of grain boundaries on fatigue crack, initiation – an energy approach. Int. J. Plast. 27, 801–821.
Stanford, N., Sha, G., Xia, J.H., Ringer, S.P., Barnett, M.R., 2011. Solute segregation and texture modification in an extruded magnesium alloy containing gadolinium. Scr. Mater. 65, 919–921.
Wang, F., Barnett, C.D., McCabe, R.J., Kadiri, H.E., Capolungo, L., Agnew, S.R., 2019. Dislocation induced twin growth and formation of basal stacking faults in {10-12} twins in pure Mg. Acta Mater. 165, 471–485.
Wang, F., Sandlöbes, S., Diehl, M., Sharma, L., Roters, F., Raabe, D., 2014a. In situ observation of collective grain-scale mechanics in Mg and Mg–rare earth alloys. Acta Mater. 80, 77–93.
Wang, H., Boehlert, C.J., Wang, Q.D., Yin, D.D., Ding, W.J., 2016. In-situ analysis of the tensile deformation modes and anisotropy of extruded Mg–10Gd–3Y–0.5Zr (wt.%) at elevated temperatures, Int. J. Plast. 84, 255–276.
Wang, J., Beyerlein, I.J., Tomé, C.N., 2014b. Reactions of lattice dislocations with grain boundaries in Mg: Implications on the micro scale from atomic-scale calculations. Int. J. Plast. 56, 156–172.
Wang, L., Yang, Y., Eisenlohr, P., Bieler, T.R., Crimp, M.A., Mason, D.E., 2010. Twin nucleation by slip transfer across grain boundaries in commercial purity titanium. Metall. Mater. Trans. A 41, 421–430.
Wang, L., Zheng, Z., Phukan, H., Kenesei, P., Park, J.-S., Lind, J., Suter, R.M., Bieler,

T.R., 2017. Direct measurement of critical resolved shear stress of prismatic and basal slip in polycrystalline Ti using high energy X-ray diffraction microscopy. Acta Mater. 132, 598–610.
Wang, Y., Srolovitz, D.J., Rickman, J.M., LeSar, R., 2000. Dislocation motion in the presence of diffusing solutes: A computer simulation study. Acta Mater. 48, 2163–2175.
Xu, X., Lunt, D., Thomas, R., Babu, R.P., Harte, A., Atkinson, M., Fonseca, J.Q. da, Preuss, M., 2019. Identification of active slip mode in a hexagonal material by correlative scanning electron microscopy, Acta Mater. 175, 376–393.
Xin, R.L., Liu, Z., Sun, Y.J., Wang, H.M., Guo, C.F., Ren, W.J., Liu, Q., 2019. Understanding common grain boundary twins in Mg alloys by a composite Schmid factor Int. J. Plast. 123, 208–223.
Zhang, C., Balachandran, S., Eisenlohr, P., Crimp, M.A., Boehlert, C., Xu, R., Bieler, T.R., 2018. Comparison of dislocation content measured with transmission electron microscopy and micro-Laue diffraction based streak analysis. Scr. Mater. 144, 74–77.
Zhang, D.L., Wen, H.M., Kumar, M.A., Chen, F., Zhang, L.M., Beyerlein, I.J., Schoenung, J.M., Mahajan, S., Lavernia, E.J., 2016. Yield symmetry and reduced strength differential in Mg–2.5Y alloy. Acta Mater. 120, 75–85.
Zhao, C.Y., Chen, X.H., Pan, F.S, Wang, J.F., Gao, S.Y., Tu ,T., Liu, C.Q., Yao, J.H., Atrens, A., 2019. Strain hardening of as-extruded Mg–xZn (x = 1, 2, 3 and 4 wt.%) alloys. J. Mater. Sci. Technol. 35, 142–150.
Zhou, B., Wang, L., Liu, W., Wang, J., Zeng, X., Ding, W., 2019. Study of the dislocation activity in a Mg–Y alloy by differential aperture X-ray microscopy. Mater. Charact. 156, 109873.
Zhu, G., Wang, L., Zhou, H., Wang, J., Shen, Y., Tu, P., Zhu, H., Liu, W., Jin, P., Zeng, X., 2019. Improving ductility of a Mg alloy via non-basal <a> slip induced by Ca addition. Int. J. Plast. 120, 164–179.